

# Effect of ROCK Pathway Manipulation on Actin Cytoskeleton Architecture: The Third Dimension

**Carolin Grandy**

University Ulm

**Fabian Port**

University Ulm

**Jonas Pfeil**

University Ulm

**Kay-Eberhard Gottschalk** (✉ [kay.gottschalk@uni-ulm.de](mailto:kay.gottschalk@uni-ulm.de))

University Ulm

---

## Research Article

**Keywords:** cytoskeleton, biochemical processes, metal-induced energy transfer (MIET), nanometer

**Posted Date:** June 28th, 2021

**DOI:** <https://doi.org/10.21203/rs.3.rs-646017/v1>

**License:**  This work is licensed under a Creative Commons Attribution 4.0 International License.

[Read Full License](#)

---

# Abstract

The actin cytoskeleton with its dynamic properties serves as the driving force for the movement and division of cells and gives the cell shape and structure. Disorders in the actin cytoskeleton occur in many diseases. Deeper understanding of the regulation is essential in order to better understand these biochemical processes. In our study, we use metal-induced energy transfer (MIET) as a tool to quantitatively examine the rarely considered third dimension of the actin cytoskeleton with nanometer accuracy. In particular, we investigate the influence of different drugs acting on the ROCK pathway on the three-dimensional actin organization. We find that cells treated with inhibitors have a lower actin height to the substrate while treatment with a stimulator for the ROCK pathway increases the actin height to the substrate. This reveals the precise tuning of adhesion and cytoskeleton tension, which leads to a rich three-dimensional structural behaviour of the actin cytoskeleton. This finetuning is differentially affected by either inhibition or stimulation.

## Statement Of Significance

The ROCK signalling pathway influences various cellular functions by acting on the cytoskeleton. However, the effect of ROCK-intervention on actin architecture needs further investigation: high-resolution structural information about actin height is lacking. The high axial resolution provided by metal-induced energy transfer (MIET) allows us to precisely measure the height of cytoskeletal structures. We show that early inhibition of the ROCK pathway leads to low structures, while later inhibition has little overall effect on the actin structure but flattens actin arches. In contrast, activating drugs cause actin to be contracted upwards. MIET hence gives unprecedented insight into three-dimensional actin regulation by the ROCK-pathway, enabling the investigation of the fine-tuned balance between adhesion tension, stress fiber formation and force generation.

## Introduction

The cells cytoskeleton gives mechanical support, allows the cell to deliver cargo and is fundamental for cell division. It consists of three biological polymers: microtubules, intermediate filaments and actin. The actin cytoskeleton is predominantly responsible for cellular movement. It is tightly regulated and highly dynamic. Actin is located in a variety of areas of the cell (Fig. 1a). It is found in the cell cortex to give the cell strength and shape [1]. To divide cells, it also forms the contractile ring around the nucleus [2,3]. For motility, it forms microvilli [4], lamellipodia and filopodia [5–8].

The actin cytoskeleton can create contractile forces in the cell. Contractile forces are generated when actin filaments recruit myosin II motor proteins [8,9]. The poly-protein complex of contractile bundles of actin filaments with myosin II molecules are called stress fibers [10]. In contrast, protrusive forces arise from the coordinated polymerisation of multiple actin filaments. Gradients of tension induce local contractions and force cell movements and deformations. [8,9]. These forces are not only important in cell migration, but also play a role in determining cell shape, adapting to the mechanical properties of the

environment, determining intracellular movement [11] and morphogenesis of membrane organelles [12]. Filamentous actin (f-actin) is also involved in the generation of mechanical forces which stimulate the differentiation and development of stem cells [13].

Regulated polymerization and depolymerization of actin monomers to polymers leads to a dynamic assembly and disassembly of actin fibers, which ensures quick cellular adaptation to changes in environment [11,14]. The small Rho GTPase RhoA is a major regulator of the cytoskeleton (Fig. 1B). It activates the Rho-associated coiled coil-containing protein kinase (ROCK) [15]. Through a positive feedback loop, ROCK directly catalyses myosin light chain phosphorylation and inhibits myosin light chain phosphatase [16]. This increases the binding of myosin II to actin and thus the contractility of the cell. ROCK also phosphorylates LIM kinase (LIMK), which then phosphorylates cofilin [17]. This deactivates actin depolymerization and the existing actin filaments are stabilized and increase in length.

High expression of ROCK/LIMK/Cofilin and other members of the ROCK pathway have been identified in cancers such as breast, prostate, colorectal and bladder [18–21]. In tumour cells, increased movement, invasion and metastasis also occur due to the actin cytoskeleton and its adaptation [8]. Viruses modify cells and the actin to best suit their hosts and proliferate [22,23]. Cell movement through the actin cytoskeleton plays a critical role in many pathologies. During chronic inflammatory diseases migration of immune cells is important [24,25] and actin dynamics are a target for therapeutics against chronic kidney diseases [26]. Ageing processes also change the actin expression and dynamics [27]. Therefore, actin modifications are involved in ageing, cancer, vascular diseases, and neurodegenerative diseases like Alzheimer's disease [27,28]. Disrupted functioning of actin is also observed in somatic cells, stem cells and gametes [13,27]. This underlines the necessity to gain a deep understanding of the Rock pathway on actin structure. In the past, a variety of high resolution fluorescence studies described the actin organization with high precision in two dimensions [29–31]. However, the third dimension, perpendicular to the focal plane, is more difficult to resolve with nanometer resolution. Metal induced energy transfer is a tool that facilitates a high precision analysis of this third dimension.

With metal induced energy transfer (MIET) as a tool, the position of fluorescent molecules above a metal surface can be determined with nanometer precision [32–35]. The principle of MIET compares best to Förster Resonance Energy Transfer (FRET). In FRET the energy of an excited donor dye is transferred to a second dye, the acceptor [36,37]. However, at MIET, the acceptor molecule is replaced by a metal layer. This results in a distance-dependent energy transfer rate between the metal layer and the donor molecules, which can directly be correlated to the fluorescence lifetime[32] and is observable at distances from the metal of more than 100 nm. The effect is based on strong optical near-field coupling of surface plasmons in a thin metal layer [33]. The fluorescence lifetime increases non-linearly with increasing distance to the metal layer and asymptotically reaches the lifetime of a free fluorophore without metal layer [32,34]. The fluorescence lifetime can hence be converted to a distance value using a calibration curve to obtain super-resolution in the Z dimension [32]. MIET imaging has already been used to study the cell mechanics of human mesenchymal stem cells [34], to better understand human blood platelet spreading[38] and for the examination of microtubules[39] and the nuclear envelope [40].

In this study, we investigate the regulation of the actin cytoskeleton through different targeting sites in the ROCK pathway. To this end, we use Blebbistatin as a myosin II inhibitor [41], Y27632 as an inhibitor for ROCK[42,43] and the Rho Activator II, which increases the activity of RhoA [44,45]. We use MIET to quantitatively observe the height of actin stress fibers and the actin cortex within nanometer accuracy. With this, we gain a better understanding of the structure of the actin cytoskeleton in the third dimension and thereby the influence of the different key points of the ROCK Pathway and their impacts on the three-dimensional actin structure. Figure 1A shows a sketch of an adherent cell with its actin cytoskeleton (red). In this work, we analyze both stress fibers, which are formed with the aid of myosin II, and the actin edge (blue), which is composed of various actin components such as cortical actin as well as stress fibers. In addition, the gradient of actin height along the actin edge is analyzed. Our results show that by treatment with Rho Activator, actin distance to the substrate is higher and distributed on a smaller projected cell area. In contrast to this, the treatment with the inhibitor Y27632 leads to lower actin heights. Blebbistatin, which only affects myosin II activity but does not directly interfere with the actin assembly pathway, does not lead to major changes in height, but flattens the actin edge of the cell. Our results indicate that there is a precise balance between adhesion tension and cytoskeleton tension of the actin cytoskeleton regulating the three-dimensional architecture. A disturbance of this balance disrupts the finely balanced interplay of forces and leads to flattened actin architecture.

## Results

The major goal of this study was the examination of the distance from the substrate to the actin cytoskeleton, a parameter we call “actin height”. We analyzed the height of a) all actin components together; b) the height of actin stress fibers; and c) the height of the actin edge – the outer edge of the actin in the cell – separately (Fig. 2). Further, we analyzed d) the gradient of the actin height along the edge of the cell, a parameter that shows us the roughness of the cell edge. Figure 2 shows in first column representative images generated via Fluorescence Lifetime Imaging Microscopy (FLIM). Using a previously created calibration curve, the fluorescence lifetimes were converted into height values[32,33,35,46,47] to get intensity-weighted height image as described in Methods. In order to also get specific height information about stress fibers, a stress-fiber specific mask was generated unbiased via the TWOMBLI plugin [48]. For further analysis of the actin cortex, the actin edge was extracted from the height image of all components. To examine the regulation of actin by the pathway, untreated cells (Fig. 2a) were treated with different drugs. Blebbistatin inhibits Myosin II (Fig. 2b), Y27632 inhibits ROCK (Fig. 2c) and the Rho Activator increases the activity of RhoA (Fig. 2d).

### Height distribution of all actin components

From the intensity weighted height images (Fig. 2b), the median height of each cell's actin components was evaluated (Fig. 3a). Untreated cells have a median of  $114 \pm 12$  nm. Cells treated with the ROCK inhibitor Y27632 show the lowest median at  $97 \pm 15$  nm, followed by cells treated with the Myosin inhibitor Blebbistatin at  $110 \pm 17$  nm. No significant difference between Blebbistatin treated cells and

untreated cells can be found. Significantly, Rho Activator treated cells show the highest median at  $124 \pm 12$  nm.

### Height distribution of stress fibers

The median of the stress fiber heights of each cell (Fig. 3b) shows a significant difference of the Rho Activator population with a median of  $132 \pm 10$  nm compared to all other populations. This is even higher ( $+ \approx 10$  nm) compared to the median of the total actin of the Rho Activator population (Fig. 3a), indicating a significant upshift of the stress fibers compared to other actin structures. The height of stress fibers of Y27632 treated cells are clearly shifted to lower heights compared to untreated cells. Despite a higher median of the height of actin stress fibers in Blebbistatin treated cells, there is no significant difference between Blebbistatin and Y27632 treated cells or between Blebbistatin-treated and untreated cells. The MIET data reveal that untreated cells (Fig. 2, 4a) have arch-like structures between the adhesion points. The Blebbistatin (Fig. 2, 4b) treated cells show an overall similar architecture. The Y27632 treated cell contains very few stress fibers and has very limited actin overall. The few stress fibers show arch-like structures (Fig. 2, 4c). The Rho Activator cell (Fig. 2, 4d) has actin stress fibers at a higher height. The stress fibers, however, show no arch-like features.

We further compared the height of the lowest and highest stress fiber regions. To this end, we extracted the regions corresponding to the 10th percentile and 90th percentiles for each of the cells (Fig. 3c, d, e, f). This is a measure of the three-dimensional height distribution: highly curved actin structures will display a larger difference between the percentiles than flat actin structures. For untreated cells, the 10th percentile is at  $90 \pm 10$  nm, while the 90th percentile is at  $147 \pm 11$  nm. This leads to a rise of the actin arches of  $56 \pm 7$  nm and a relative rise of  $38 \pm 4$  %. Blebbistatin shows no significant difference compared to untreated cells. The Rho Activator treated cells have a significantly higher 10th percentile at  $106 \pm 12$  nm and  $157 \pm 9$  nm for the 90th percentile. Its actin arcs increase with  $50 \pm 6$  nm and have a relative rise of  $32 \pm 5$  %. Y27632 treated cells, on the other hand, have significantly lower heights in the 10th percentile at  $106 \pm 12$  nm, but are not different compared to Blebbistatin treated and untreated cells in the 90th percentile with  $146 \pm 15$  nm. However, they show differences in the rise of actin arches of  $59 \pm 7$  nm and have a relative rise of  $42 \pm 5$  %.

### Actin border analysis

Cell deformations must be precisely controlled as they are key to cell migration, differentiation, division and tissue morphogenesis. These parameters play a significant role in carcinogenesis [49,50]. Changes in cell shape are driven by tension gradients in the cellular cortex [51]. This consists of a thin actomyosin network formed by cortical actin and stress fibers in addition to actin mesh [49–51]. To gain deeper insight into this important outer edge of the cellular cytoskeleton, the height behaviour at the boundary of these actin structures is analyzed.

Due to the high axial resolution, Y27632 treated cells (Fig. 5a) were discovered to have the lowest height ( $103 \pm 15$  nm) of all conditions. In contrast, the actin cytoskeleton of Rho Activator treated cells is shifted

to higher heights, while the actin edge of untreated ( $116 \pm 13$  nm) and Blebbistatin treated cells ( $114 \pm 18$  nm) have a similar median.

In addition to analyzing the height of the actin and the influence of the drugs on it, the derivative of the edge height along the edge (Fig. 5b) was also analyzed. For further analysis of the steepness distribution of the actin edge, we analyzed the slope of the edge according to its gradient angle defined by

$\theta = \arctan \frac{\partial h}{\partial x}$ , where dh is the change in height of a lateral distance dx. Blebbistatin ( $3.0 \pm 0.5^\circ$ ) and Y27632 ( $3.0 \pm 0.8^\circ$ ) treated cells show a similar overall median and significantly lower gradient angles compared to untreated and Rho activator treated cells, respectively. There is no significant difference between untreated and Rho Activator treated cells. However, untreated cells have a broader distribution and higher variation compared to cells treated with the Rho Activator.

By correlating the heights of the actin edge with the gradient angle along the edge untreated cells (Fig. 5c) show the widest distribution of angles. The highest density and thus the most heights occur between 95 and 140 nm with a tangent angle of  $3.3 \pm 1.1^\circ$ . Blebbistatin (Fig. 5e) and Y27632 (Fig. 5f) treated cells show a similar and very broad height distribution especially concentrated in the range of 70 to 130 nm. They occur mainly concentrated at low heights with a tangent angle of  $3.0 \pm 0.5^\circ$  (Blebbistatin) and  $3.0 \pm 0.8^\circ$  (Y27632). Y27632 cells, however, have slightly lower heights compared to Blebbistatin treated cells. Blebbistatin cells display two centres of high density. Both populations show similar angles. Lower angles are also more likely to be found at lower heights. The Rho Activator cells (Fig. 5d), on the other hand, are clearly shifted to the higher heights. The highest density occurs in the range from 110 to 150 nm. They show more evenly distributed angles than untreated cells.

Table 1 provides a summary (median  $\pm$  std) of the analysis of the actin cytoskeleton in z dimension using MIET, as well as the gradient angles along the actin edge.

Table 1  
Summary of the medians  $\pm$  std from height and angle analyses of the actin cytoskeleton of untreated cells and cells treated with Blebbistatin, Y27632 and Rho Activator.

Median	Untreated	Blebbistatin	Y27632	Rho Activator
Height of Actin (nm)	$114 \pm 12$	$110 \pm 17$	$97 \pm 15$	$124 \pm 12$
Stress Fiber Height (nm)	$118 \pm 12$	$122 \pm 17$	$112 \pm 13$	$132 \pm 10$
Relative Stress Fiber Rise	$0.38 \pm 0.04$	$0.36 \pm 0.05$	$0.42 \pm 0.05$	$0.32 \pm 0.05$
Height of Actin Edge (nm)	$116 \pm 13$	$114 \pm 18$	$103 \pm 15$	$130 \pm 12$
Gradient Angle along Actin Edge ( $^\circ$ )	$3.3 \pm 1.1$	$3.0 \pm 0.5$	$3.0 \pm 0.8$	$3.4 \pm 0.5$

#### Analysis of actin in the focal plane

Interestingly, the treatment with the respective drugs leads to changes in total cell area. A significantly smaller cell area for the Rho Activator (Fig. 6a) cells compared to the other three populations can be seen.

The cells treated with Y27632 have a significantly larger actin cell area than untreated and Blebbistatin treated cells. Furthermore, to see how sparse the actin cytoskeleton is and in which ratio the actin is distributed in the cell, the actin area of the fibers obtained using the TWOMBLI plugin was normalised to the cell area (Fig. 6b). The Y27632 treated cells have a significantly larger cell area with a low actin content. In contrast the Rho Activator treated cells have a small cell area with a high actin content.

## Discussion

Many diseases like cancer, involve the ROCK pathway, which also affect the actin cytoskeleton [18–21]. Therefore, a deeper understanding of the impact of this pathway on actin organization is of major concern. Previous structural studies predominantly analyzed the actin regulation and the interaction with the ROCK pathway in the two dimensions of the focal plane [52,53]. Mostly due to technical difficulties, the third dimension normal to the focal plane has been examined to a far lesser extent. The three-dimensional structure of actin is important for a thorough understanding of cellular physiology and pathophysiology. For this reason, we analyzed here the third dimension in nanometer resolution using MIET. Previously, Chizhik et al.[34] studied the height distribution of actin stress fibers of human mesenchymal stem cells on gold-coated glass at specific time points. In our study, we examined differentiated embryonic mouse fibroblasts using fibronectin as substrate coating. The average actin height appears to be different in the two studies: while in our study, the 10 percentile lowest structures are in the range of 80 nm – 120 nm, the earlier study finds lowest actin heights in the order of 20 nm – 40 nm. In contrast to this, the actin heights of embryonic mouse fibroblasts from Kanchanawong et al.[54] compares well to our measured height results. Hence, the height profile may be cell type dependent.

Chizhik et al. focus on the time evolution of stress fibers, while here, we concentrate on the effect of disturbing the ROCK pathway on actin height distributions. To this end, we just used end-point measurements of cells seeded after 24 h. We find profound and novel effects of actin regulatory drugs on the height and architecture of the actin structures. In particular, inhibition at an early point in the ROCK pathway leads to a lowering of actin height, while activation leads to an increase in actin height. These differences in height may be caused by re-structuring of the connection between cytoskeleton and extracellular matrix, so called focal adhesions. Integrins expressed on the cell surface bind to the RGD binding motif on fibronectin and may exert forces, depending on ROCK intervention. Fibronectin has been shown to dynamically alter its fibrous structure depending on external forces, revealing cryptic binding sites [55–57]. This may lead to force dependent, integrin-mediated re-organization of the cytoskeleton and to recruitment of further proteins to the focal adhesions[58,59] above a certain force threshold [60]. Recruiting more proteins to re-enforce the connection would lead to higher actin structures in line with our results here. Further studies are necessary to understand this mechanism.

The height resolution offered by MIET allows us not only to determine the height of the structures, but also to calculate inclination angles along actin borders. Chizhik et al. find very low inclination angles of

actin stress fibers on the order of  $0.15^\circ$  distinct from our values of around  $3^\circ$ . However, we measure different structures: while the previous paper investigates specific pre-chosen stress fibers, we focus on the edge of actin. This edge is comprised of different actin structures like cortical actin and stress fibers. Here, it is interesting to observe mainly an effect of inhibitors: these lead to lower angles, while activators hardly change this angle compared to untreated cells.

In order to understand the behaviour of the actin cytoskeleton in the ROCK pathway (Fig. 1a) in the focal plane as well as in the z-dimension, we adopt a simple model previously described [61,62]. It relates the balance between cytoskeleton tension and adhesion tension. Cytoskeletal tension pulls the cell upwards and rounds it up. Balancing this force is the adhesion tension, which tends to stretch the cell. Figure 7 shows a possible model for the relationship between adhesion tension and cytoskeleton tension to describe the analyzed height behaviour in relation to the ROCK pathway.

Untreated cells form arch like actin fibre structures with a ruffled actin edge. When Blebbistatin is added after formation of the actin stress fibers, only small changes can be observed. However, the ruffled actin edge becomes flattened, showing that the ruffling requires active force generation by the cell, since treatment of the cells with Blebbistatin directly inhibits myosin II activity.

As opposed to Blebbistatin, Y27632 does not directly inhibit myosin II, which appears later in the ROCK pathway, but rather inhibits ROCK, which is an important key point in the pathway. By inhibiting ROCK, less myosin light chain is phosphorylated and thus less myosin II is available for stress fiber formation and maintenance of stress fiber tension. In addition, inhibiting ROCK prevents cofilin phosphorylation by LIM kinase. Non-phosphorylated cofilin depolymerizes existing actin and leads to an active degradation of actin. Therefore, there is barely any cytoskeleton tension in the Y27632 treated cells due to the destruction of actin and the lack of stress fibers. The adhesion tension predominates in the previously existing equilibrium. This results in significant wide spreading of the cells and lowering of the actin structures. Interestingly, the actin stress fibers appear to be so weak, that even the reduced myosin II induced tension is sufficient for increased arching of the actin stress fibers. The comparison of Blebbistatin and Y27632 clearly shows that although both drugs act similarly, the effect on the actin structure is drastically different.

Cells treated with the Rho Activator show an opposite effect to cells treated with inhibitors. The Rho Activator increases the activity of RhoA, which in turn increases the activity of ROCK. The myosin light chain is increasingly phosphorylated. In addition, a positive feedback loop inhibits myosin light chain phosphatase. More myosin II is provided for stress fiber formation and maintenance of existing stress fibers. This results in stronger contractions in the cytoskeleton compared to untreated cells. Furthermore, the increased activity of ROCK also causes the LIM kinase to phosphorylate more cofilin. As a result, less actin is depolymerized and existing actin structures are stabilized. Thereby, the actin content is increased to an even greater extent. Due to this stabilization of existing actin structures and the stronger contraction, the cytoskeleton tension increases strongly. This creates an imbalance, causing the actin cytoskeleton to be pulled further up and together leading to rounded shape with a small area and high

concentration of actin fibers. The reduced migration behaviour described in the literature [17,63] can also be explained by this imbalance.

As shown in this study, the regulation of the ROCK pathway has an effect not only on the actin cytoskeleton at the focal plane but also perpendicular to it. However, cell-to-cell variations in shape and size make an even deeper analysis of the effect of these drugs challenging.

In summary, we show that balancing forces in the actin cytoskeleton is required for a proper three-dimensional cytoskeletal architecture. Increasing tension leads to an actin cytoskeleton at large height in cells with a small cross-sectional area, while decreasing cytoskeletal tension also flattens the actin cytoskeleton but close to the cell's substrate with increased cell area.

## Materials And Methods

### Coating for MIET measurements

For MIET measurements glass coverslips (Paul-Marienfeld, Lauda-Königshofen, Germany) were silanized by evaporation with (3-Mercaptopropyl)trimethoxysilane (MPTMS) (Sigma-Aldrich, Darmstadt, Germany) and afterwards coated with 20 nm gold (Kurt-Lesker) as previously described [64].

To apply fibronectin to the gold surfaces, the gold slides were treated with the crosslinker Dithiobis (succinimidyl propionate) (DSP) (Thermo-Fisher, Waltham, Massachusetts, USA) in Dimethyl sulfoxide (DMSO) (4 mg/mL) for 30 min.

Afterwards coverslips were washed in Phosphate buffered saline (PBS) and coated with 0.025 mg/mL fibronectin (Sigma-Aldrich, Darmstadt, Germany) for 2 h. Fibronectin as an extracellular matrix protein is used to bind fibroblasts to integrins via its RGD sequence.

### Cell Culture, drug treatment and immunofluorescence staining

NIH 3T3 mice fibroblasts (ATCC® CRL-1658™, Manassas, Virginia, USA) were cultured in Dulbecco's Modified Eagle Medium (Gibco by life technologies, Germany) containing 10% Fetal Bovine serum (Bio&Sell, Feucht, Germany) and 1% Antibiotic/Antimycotic solution (GE Healthcare Hyclone, Chicago, Illinois, USA). For MIET measurements cells were trypsinized with Trypsin/EDTA (Biowest, Nuaillé, France) for 3 min and seeded on fibronectin coated gold coverslips for 24 h in the incubator.

The cells were treated with different drugs the next day. Drug treatment was 50 µM Blebbistatin (Sigma-Aldrich, Darmstadt, Germany) for 40 min, 10 µM Y-27632 (Sigma-Aldrich, Darmstadt, Germany) for 1 h and 1 µg/µL Rho-Activator II (Cytoskeleton, Denver, CO, USA) for 3 h, respectively. After each drug treatment cells were briefly rinsed 3x in PBS, which was immediately removed and then fixed in 4% formaldehyde (Polysciences, USA) for 10 min.

For immunofluorescence staining cells were permeabilized in 0.8% Triton X-100 (Sigma-Aldrich, Darmstadt, Germany. For blocking they were incubated in 0.1 M Glycin (Alfa Aesar, Haverhill, Massachusetts, USA) for 30 min and 3% Bovine serum album (Sigma-Aldrich, Darmstadt, Germany) for 30 min. To stain the Golgi apparatus, incubation was performed for 3 h in the primary golgin-97 polyclonal antibody 6.7 µg/mL (Thermo Fisher Scientific, Waltham, Massachusetts, USA) and 3 h in the secondary goat anti-rabbit Alexa fluor 488 antibody 4 µg/mL (Thermo Fisher Scientific, Waltham, Massachusetts, USA). The actin cytoskeleton was stained by incubating 66 µM Alexa Fluor 568 phalloidin (Thermo Fisher Scientific, Waltham, Massachusetts, USA) overnight. The nucleus was stained with DAPI (AppliChem, Darmstadt, Germany) in a concentration of 0.002 µg/mL for 5 min. Except of the overnight staining at 4°C all steps of immunofluorescence staining are performed at room temperature. For imaging PBS was used as mounting medium.

## Experimental setup

MIET measurements are performed on a fluorescence lifetime imaging microscopy setup MicroTime 200 of PicoQuant (Berlin, Germany). The setup is attached to an inverted microscope Olympus IX73 (Hamburg, Germany). Fluorophores are excited via a pulsed diode laser (LDH-D-TA-560, pulse width ~ 56 ps, repetition rate 40 MHz, wavelength 520 nm), which is coupled into a polarization maintaining single mode fiber. For both focusing excitation light and collecting fluorescence light a high numerical aperture objective (60x1.2 UPlanSApo, Superapochromat, water immersion, WD = 0.28 mm) was used. The collected fluorescence has been splitted by a dichroic beam splitter (zt488/861rpc-UF3, AHF/Chroma, Tübingen, Germany), passing the pinhole and is filtered by an emission short-pass ET750sp-2p8 (AHF/Chroma, Tübingen, Germany) and emission long-pass filter BLP01-594R (AHF/Chroma, Tübingen, Germany) to the hybrid-PMT detector. For data acquisition the multichannel picosecond event timer HydraHarp 400 TCSPC module of PicoQuant (Berlin, Germany) was used. FLIM images of each single cell were recorded with the SymPhoTime 64 software (PicoQuant, Berlin, Germany).

## Fluorescence lifetime data evaluation

Fluorescence photons were detected in time-tagged, time-resolved mode, which makes it possible to collect all photons of single pixels and sort them into a histogram according to their arrival time after the last laser pulse. A multi-exponential deconvolution fit with a self-recorded IRF was applied to the data sets in the SymPhoTime 64 software (PicoQuant, Berlin, Germany).

## Converting lifetime to height values

The MIET GUI programme of the Enderlein group (University of Göttingen) in MATLAB was used to generate the calibration curve to get the height data from the lifetime data. The theory of how to generate the height data from the lifetimes was described in detail previously [32,33,35,46,47]. The layers of the MIET samples were all of the same composition. On the bottom of the sample was glass (refractive index  $n = 1.52$ ) and a layer of MPTMS ( $n = 1.443$  [65]), which was coated with 20 nm of gold. The refractive index of gold is wavelength-dependent and was taken from [66]. Above the gold is the cell ( $n = 1.36$  [67]).

and PBS ( $n = 1.33$  [68]) as mounting medium. The calibration curve was then used to calculate the height values in a custom-written MATLAB code, which was adapted from the MIET GUI [32,35].

## MATLAB height analysis

For further analysis of the calculated heights the MATLAB ver. R2019b software (The MathWorks, Inc, Natick, Massachusetts, USA) was used. In order to determine the edge of the cell, the image was binarized and the largest object was selected. The edge of the largest object corresponds to the actin edge and was calculated with pixel accuracy. To avoid binarization artefacts, the cell was eroded by 2 pixels. Areas of cells larger than the image section were not included in the edge analysis. For the determination of the gradient angle along edge, the cell height along the edge line was derived and the angle was calculated for every edge pixel accordingly. To normalize the delta of the 90th percentile to the 10th percentile of stress fiber height, a parameter we call relative stress fiber rise, the difference was divided by the 90th percentile.

## Extract stress fibers

To extract the stress fibers from the intensity weighted height images, these images were analyzed using the TWOMBLI plugin [48] in Fiji [69,70]. The resulting masks were applied to the existing datasets in MATLAB.

## Quantification and statistical analysis

The populations used for the analysis of the entire study are composed of the following number of single cells: Untreated  $N = 39$ , Blebbistatin  $N = 38$ , Y27632  $N = 39$ , Rho Activator  $N = 48$ . Plots in Fig. 2, 3, 6 are generated using MATLAB. Boxplots are generated using PlotsOfData [71]. For statistical analysis Wilcoxon-rank-sum test was performed in MATLAB. ns:  $p > 0.05$ , \*:  $p \leq 0.05$ , \*\*:  $p \leq 0.01$ , \*\*\*:  $p \leq 0.001$ , \*\*\*\*:  $p \leq 0.0001$ .

## Declarations

## Acknowledgments

The authors would like to thank Peter Kolb for the gold evaporation and Melanie Lahrkamp for illustrating the cells in figure 1 a and figure 8.

## Author contributions

C.G. performed the research, programmed the MATLAB analysis code, evaluated the data and wrote the paper. F.P. evaluated the data and programmed the MATLAB analysis code. J.P. programmed the MATLAB analysis code. K.E.G. designed the research, evaluated the data and wrote the paper.

# Declaration of interests

The authors declare no competing interests.

## Data availability statement

The datasets generated during and/or analysed during the current study are available from the corresponding author on reasonable request.

## References

1. Clark, A. G., Dierkes, K. & Paluch, E. K. Monitoring actin cortex thickness in live cells. *Biophysical journal* **105**, 570–580 (2013).
2. Fujiwara, K. & Pollard, T. D. Fluorescent antibody localization of myosin in the cytoplasm, cleavage furrow, and mitotic spindle of human cells. *J Cell Biol* **71**, 848–875 (1976).
3. Schroeder, T. E. The contractile ring. II. Determining its brief existence, volumetric changes, and vital role in cleaving Arbacia eggs. *J Cell Biol* **53**, 419–434 (1972).
4. Mooseker, M. S. & Tilney, L. G. Organization of an actin filament-membrane complex. Filament polarity and membrane attachment in the microvilli of intestinal epithelial cells. *J Cell Biol* **67**, 725–743 (1975).
5. Dale D. Tang & Brennan D. Gerlach. The roles and regulation of the actin cytoskeleton, intermediate filaments and microtubules in smooth muscle cell migration. *Respir Res* **18**, 1–12 (2017).
6. Gerthoffer, W. T. Migration of Airway Smooth Muscle Cells. *Proceedings of the American Thoracic Society* **5**, 97–105 (2008).
7. Gerthoffer, W. T. Actin cytoskeletal dynamics in smooth muscle contraction. *Canadian journal of physiology and pharmacology* **83**, 851–856 (2005).
8. Svitkina, T. The Actin Cytoskeleton and Actin-Based Motility. *Cold Spring Harbor Perspectives in Biology* **10** (2018).
9. Pollard, T. D. & Borisy, G. G. Cellular Motility Driven by Assembly and Disassembly of Actin Filaments. *Cell* **112**, 453–465 (2003).
10. Schoenwaelder, S. M. & Burridge, K. Bidirectional signaling between the cytoskeleton and integrins. *Current Opinion in Cell Biology* **11**, 274–286 (1999).
11. Pollard, T. D. & Cooper, J. A. Actin, a Central Player in Cell Shape and Movement. *Science* **326**, 1208–1212 (2009).
12. Chhabra, E. S. & Higgs, H. N. The many faces of actin: matching assembly factors with cellular structures. *Nature cell biology* **9**, 1110–1121 (2007).
13. Fan, Y.-L., Zhao, H.-C., Li, B., Zhao, Z.-L. & Feng, X.-Q. Mechanical Roles of F-Actin in the Differentiation of Stem Cells: A Review. *ACS Biomaterials Science & Engineering* **5**, 3788–3801

(2019).

14. Pantaloni, D., Le Clainche, C. & Carlier, M. F. Mechanism of actin-based motility. *Science (New York, N.Y.)* **292**, 1502–1506 (2001).
15. Leung, T., Chen, X. Q., Manser, E. & Lim, L. The p160 RhoA-binding kinase ROK alpha is a member of a kinase family and is involved in the reorganization of the cytoskeleton. *Molecular and Cellular Biology* **16**, 5313–5327 (1996).
16. Kimura, K. *et al.* Regulation of Myosin Phosphatase by Rho and Rho-Associated Kinase (Rho-Kinase). *Science* **273**, 245–248 (1996).
17. Maekawa, M. *et al.* Signaling from Rho to the Actin Cytoskeleton Through Protein Kinases ROCK and LIM-kinase. *Science* **285**, 895–898 (1999).
18. Kalender, M. E. *et al.* Association between the Thr431Asn polymorphism of the ROCK2 gene and risk of developing metastases of breast cancer. *Oncology research* **18**, 583–591 (2010).
19. Kamai, T. *et al.* Significant Association of Rho/ROCK Pathway with Invasion and Metastasis of Bladder Cancer. *Clin Cancer Res* **9**, 2632–2641 (2003).
20. Maimaiti, Y. *et al.* Overexpression of cofilin correlates with poor survival in breast cancer: A tissue microarray analysis. *Oncology Letters* **14**, 2288–2294 (2017).
21. Lee, M.-H., Kundu, J. K., Chae, J.-I. & Shim, J.-H. Targeting ROCK/LIMK/cofilin signaling pathway in cancer. *Arch. Pharm. Res.* **42**, 481–491 (2019).
22. Cudmore, S., Cossart, P., Griffiths, G. & Way, M. Actin-based motility of vaccinia virus. *Nature* **378**, 636–638 (1995).
23. Digard, P. *et al.* Modulation of nuclear localization of the influenza virus nucleoprotein through interaction with actin filaments. *Journal of virology* **73**, 2222–2231 (1999).
24. Wynn, T. A., Chawla, A. & Pollard, J. W. Macrophage biology in development, homeostasis and disease. *Nature* **496**, 445–455 (2013).
25. Davidson, A. J. & Wood, W. Unravelling the Actin Cytoskeleton: A New Competitive Edge? *Trends in Cell Biology* **26**, 569–576 (2016).
26. Sever, S. & Schiffer, M. Actin dynamics at focal adhesions: a common endpoint and putative therapeutic target for proteinuric kidney diseases. *Kidney International* **93**, 1298–1307 (2018).
27. Lai, W.-F. & Wong, W.-T. Roles of the actin cytoskeleton in aging and age-associated diseases. *Ageing research reviews* **58**, 101021 (2020).
28. Bamburg, J. R. & Bernstein, B. W. Actin dynamics and cofilin-actin rods in alzheimer disease. *Cytoskeleton (Hoboken, N.J.)* **73**, 477–497 (2016).
29. Mazloom-Farsibaf, H. *et al.* Comparing lifeact and phalloidin for super-resolution imaging of actin in fixed cells. *PLoS one* **16**, e0246138 (2021).
30. Brown, A. C. N. *et al.* Remodelling of Cortical Actin Where Lytic Granules Dock at Natural Killer Cell Immune Synapses Revealed by Super-Resolution Microscopy. *PLOS Biology* **9**, e1001152 (2011).

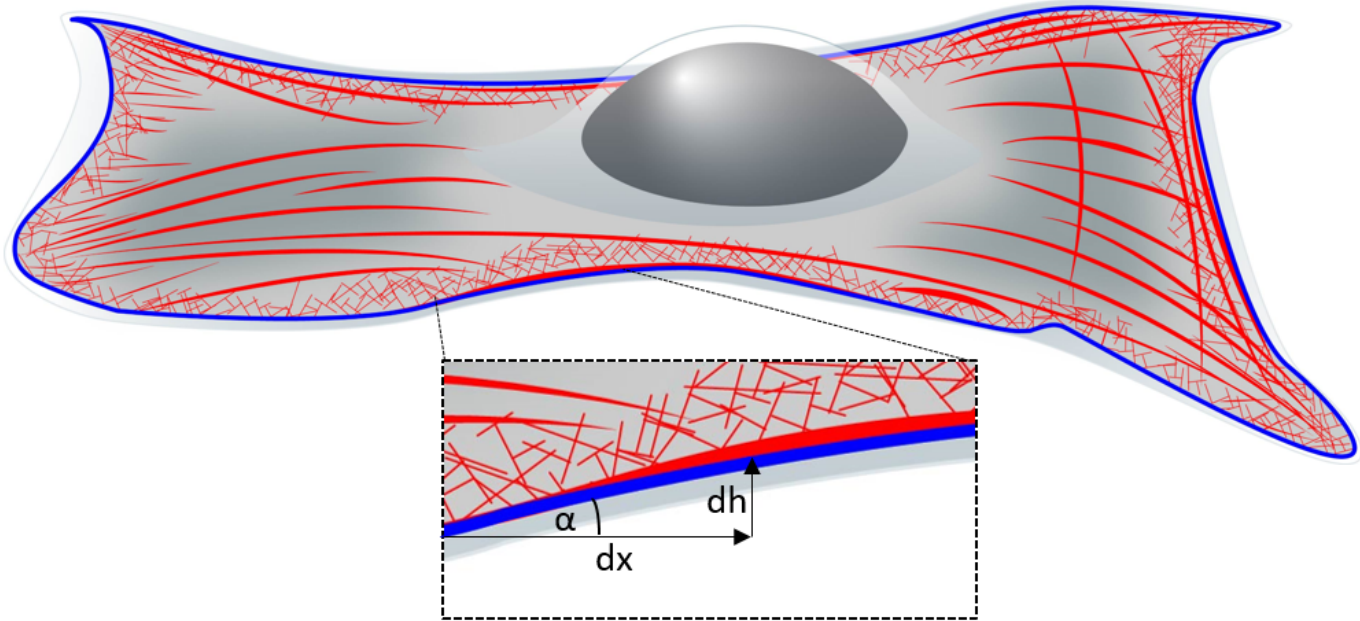
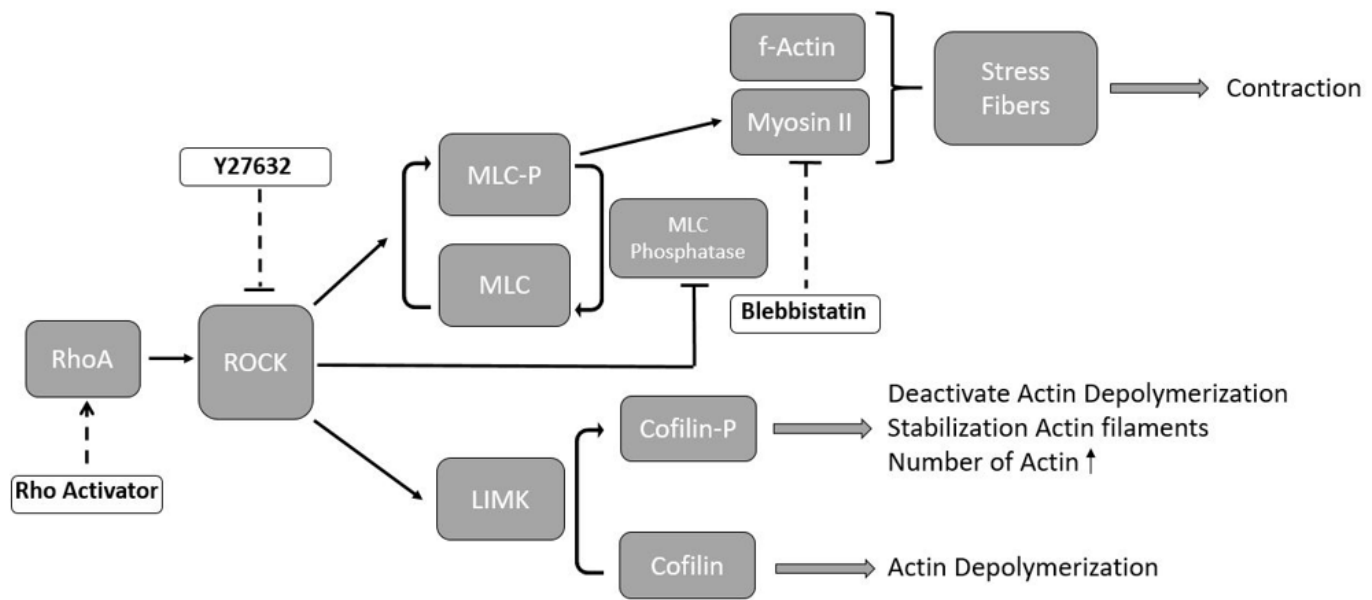
31. Sharma, S. *et al.* Correlative nanomechanical profiling with super-resolution F-actin imaging reveals novel insights into mechanisms of cisplatin resistance in ovarian cancer cells. *Nanomedicine: Nanotechnology, Biology and Medicine* **8**, 757–766 (2012).
32. Chizhik, A. I., Rother, J., Gregor, I., Janshoff, A. & Enderlein, J. Metal-induced energy transfer for live cell nanoscopy. *Nature Photon* **8**, 124–127 (2014).
33. Enderlein, J. Single-molecule fluorescence near a metal layer. *Chemical Physics* **247**, 1–9 (1999).
34. Chizhik, A. I. *et al.* Dual-Color Metal-Induced Energy Transfer (MIET) Imaging for Three-Dimensional Reconstruction of Nuclear Envelope Architecture. *Methods in molecular biology (Clifton, N.J.)* **2175**, 33–45 (2020).
35. Chizhik, A. I. & Enderlein, J. in *Nanoscale photonic imaging*, edited by T. Salditt, A. Egner & R. Luke (Springer Open, 2020), pp. 227–239.
36. Lakowicz, J. R. in *Principles of Fluorescence Spectroscopy*, edited by J. R. Lakowicz (Springer, 1999), pp. 367–394.
37. Förster, T. Zwischenmolekulare Energiewanderung und Fluoreszenz. *Ann. Phys.* **437**, 55–75 (1948).
38. Zelená, A. *et al.* Time-resolved MIET measurements of blood platelet spreading and adhesion. *Nanoscale* **12**, 21306–21315 (2020).
39. Berndt, M., Lorenz, M., Enderlein, J. & Diez, S. Axial nanometer distances measured by fluorescence lifetime imaging microscopy. *Nano letters* **10** (2010).
40. Chizhik, A. M. *et al.* Three-Dimensional Reconstruction of Nuclear Envelope Architecture Using Dual-Color Metal-Induced Energy Transfer Imaging. *ACS nano* **11**, 11839–11846 (2017).
41. Kovács, M., Tóth, J., Hetényi, C., Málnási-Csizmadia, A. & Sellers, J. R. Mechanism of blebbistatin inhibition of myosin II. *The Journal of biological chemistry* **279**, 35557–35563 (2004).
42. Ishizaki, T. *et al.* Pharmacological Properties of Y-27632, a Specific Inhibitor of Rho-Associated Kinases. *Mol Pharmacol* **57**, 976–983 (2000).
43. Uehata, M. *et al.* Calcium sensitization of smooth muscle mediated by a Rho-associated protein kinase in hypertension. *Nature* **389**, 990–994 (1997).
44. Flatau, G. *et al.* Toxin-induced activation of the G protein p21 Rho by deamidation of glutamine. *Nature* **387**, 729–733 (1997).
45. Schmidt, G. *et al.* Gln 63 of Rho is deamidated by Escherichia coli cytotoxic necrotizing factor-1. *Nature* **387**, 725–729 (1997).
46. Ghosh, A., Chizhik, A. I., Karedla, N. & Enderlein, J. Graphene- and metal-induced energy transfer for single-molecule imaging and live-cell nanoscopy with (sub)-nanometer axial resolution. *Nat Protoc*, 1–21 (2021).
47. Karedla, N. *et al.* Single-molecule metal-induced energy transfer (smMIET): resolving nanometer distances at the single-molecule level. *Chemphyschem : a European journal of chemical physics and physical chemistry* **15**, 705–711 (2014).

48. Wershof, E. *et al.* A FIJI macro for quantifying pattern in extracellular matrix. *Life science alliance* **4** (2021).
49. Vignaud, T. *et al.* Stress fibres are embedded in a contractile cortical network. *Nat. Mater.* **20**, 410–420 (2021).
50. Lehtimäki, J. I., Rajakylä, E. K., Tojkander, S. & Lappalainen, P. Generation of stress fibers through myosin-driven reorganization of the actin cortex. *eLife Sciences Publications, Ltd* (2021).
51. Chugh, P. & Paluch, E. K. The actin cortex at a glance. *J Cell Sci* **131** (2018).
52. Lee, S. H. & Dominguez, R. Regulation of actin cytoskeleton dynamics in cells. *Mol Cells* **29**, 311–325 (2010).
53. Spiering, D. & Hodgson, L. Dynamics of the Rho-family small GTPases in actin regulation and motility. *Cell Adhesion & Migration* **5**, 170–180 (2011).
54. Kanchanawong, P. *et al.* Nanoscale architecture of integrin-based cell adhesions. *Nature* **468**, 580–584 (2010).
55. Klotzsch, E. *et al.* Fibronectin forms the most extensible biological fibers displaying switchable force-exposed cryptic binding sites. *Proceedings of the National Academy of Sciences of the United States of America* **106**, 18267–18272 (2009).
56. Smith, M. L. *et al.* Force-induced unfolding of fibronectin in the extracellular matrix of living cells. *PLoS biology* **5**, e268 (2007).
57. del Rio, A. *et al.* Stretching single talin rod molecules activates vinculin binding. *Science (New York, N.Y.)* **323**, 638–641 (2009).
58. Geiger, B., Spatz, J. P. & Bershadsky, A. D. Environmental sensing through focal adhesions. *Nat Rev Mol Cell Biol* **10**, 21–33 (2009).
59. Critchley, D. R. Focal adhesions – the cytoskeletal connection. *Current Opinion in Cell Biology* **12**, 133–139 (2000).
60. Benito-Jardón, M. *et al.* The fibronectin synergy site re-enforces cell adhesion and mediates a crosstalk between integrin classes. *eLife* **6** (2017).
61. Maître, J.-L. *et al.* Adhesion functions in cell sorting by mechanically coupling the cortices of adhering cells. *Science (New York, N.Y.)* **338**, 253–256 (2012).
62. Manning, M. L., Foty, R. A., Steinberg, M. S. & Schoetz, E.-M. Coaction of intercellular adhesion and cortical tension specifies tissue surface tension. *Proceedings of the National Academy of Sciences of the United States of America* **107**, 12517–12522 (2010).
63. Riento, K. & Ridley, A. J. Rocks: multifunctional kinases in cell behaviour. *Nature reviews. Molecular cell biology* **4**, 446–456 (2003).
64. Grandy, C., Kolb, P., Port, F. & Gottschalk, K.-E. Micropatterning of Cells on Gold Surfaces for Biophysical Applications. *STAR protocols* **1**, 100106 (2020).
65. Pavlovic, E., Quist, A. P., Gelius, U. & Oscarsson, S. Surface functionalization of silicon oxide at room temperature and atmospheric pressure. *Journal of colloid and interface science* **254**, 200–203

(2002).

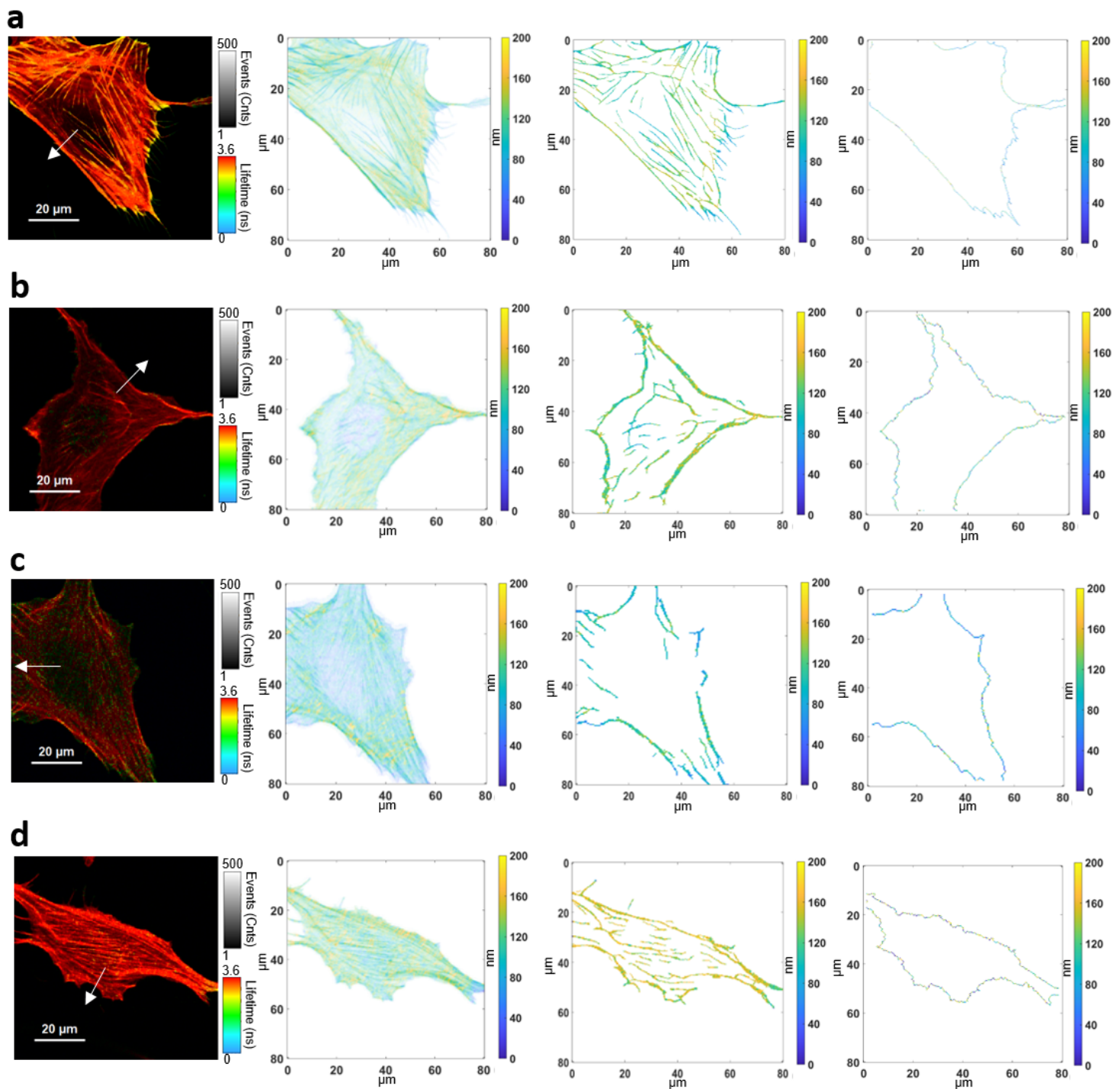
66. Rakic, A. D., Djurisic, A. B., Elazar, J. M. & Majewski, M. L. Optical properties of metallic films for vertical-cavity optoelectronic devices. *Applied optics* **37**, 5271–5283 (1998).
67. Curl, C. L. *et al.* Refractive index measurement in viable cells using quantitative phase-amplitude microscopy and confocal microscopy. *Cytometry. Part A : the journal of the International Society for Analytical Cytology* **65**, 88–92 (2005).
68. van Hoang, T. *et al.* Optical Properties of Buffers and Cell Culture Media for Optofluidic and Sensing Applications. *Applied Sciences* **9**, 1145 (2019).
69. Schneider, C. A., Rasband, W. S. & Eliceiri, K. W. NIH Image to ImageJ: 25 years of image analysis. *Nature methods* **9**, 671–675 (2012).
70. Schindelin, J. *et al.* Fiji: an open-source platform for biological-image analysis. *Nature methods* **9**, 676–682 (2012).
71. Postma, M. & Goedhart, J. PlotsOfData—A web app for visualizing data together with their summaries. *PLOS Biology* **17**, e3000202 (2019).

## Figures

**a****b****Figure 1**

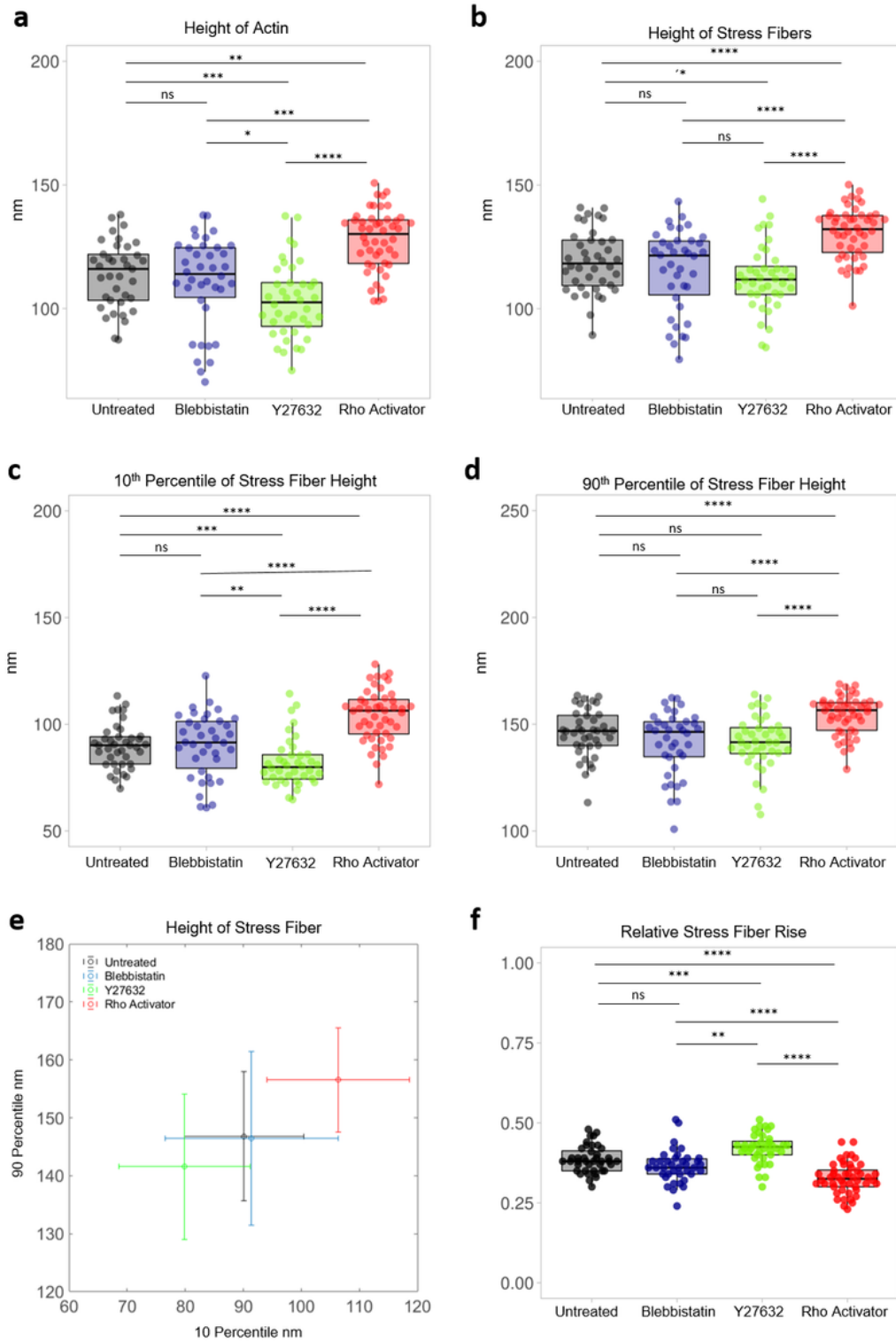
a. Scheme of a cell with actin cytoskeleton (red) and nucleus (grey) shown in 3D. The further analyzed actin edge consists of different types of actin and is shown in blue. The image section shows the parameter angle along the edge, which describes the differentiation of the edge. b. Schematic of the investigated ROCK Pathway and the influence of certain drugs on key points in the pathway. RhoA activates the Rho-associated coiled coil-containing protein kinase (ROCK). ROCK catalyzes the

phosphorylation of the myosin light chain (MLC) to myosin light chain phosphate (MLC-P) and inhibits myosin light chain phosphatase (positive feedback loop). This increases the binding of myosin II to actin and thus the contractility of the cell increases. ROCK phosphorylates LIM kinase (LIMK). This phosphorylates cofilin. The existing actin filaments stabilize and increase as actin depolymerization is deactivated. Rho activator enhances the action of RhoA, Y27632 directly inhibits ROCK in the pathway and Blebbistatin inhibits the action of myosin II.



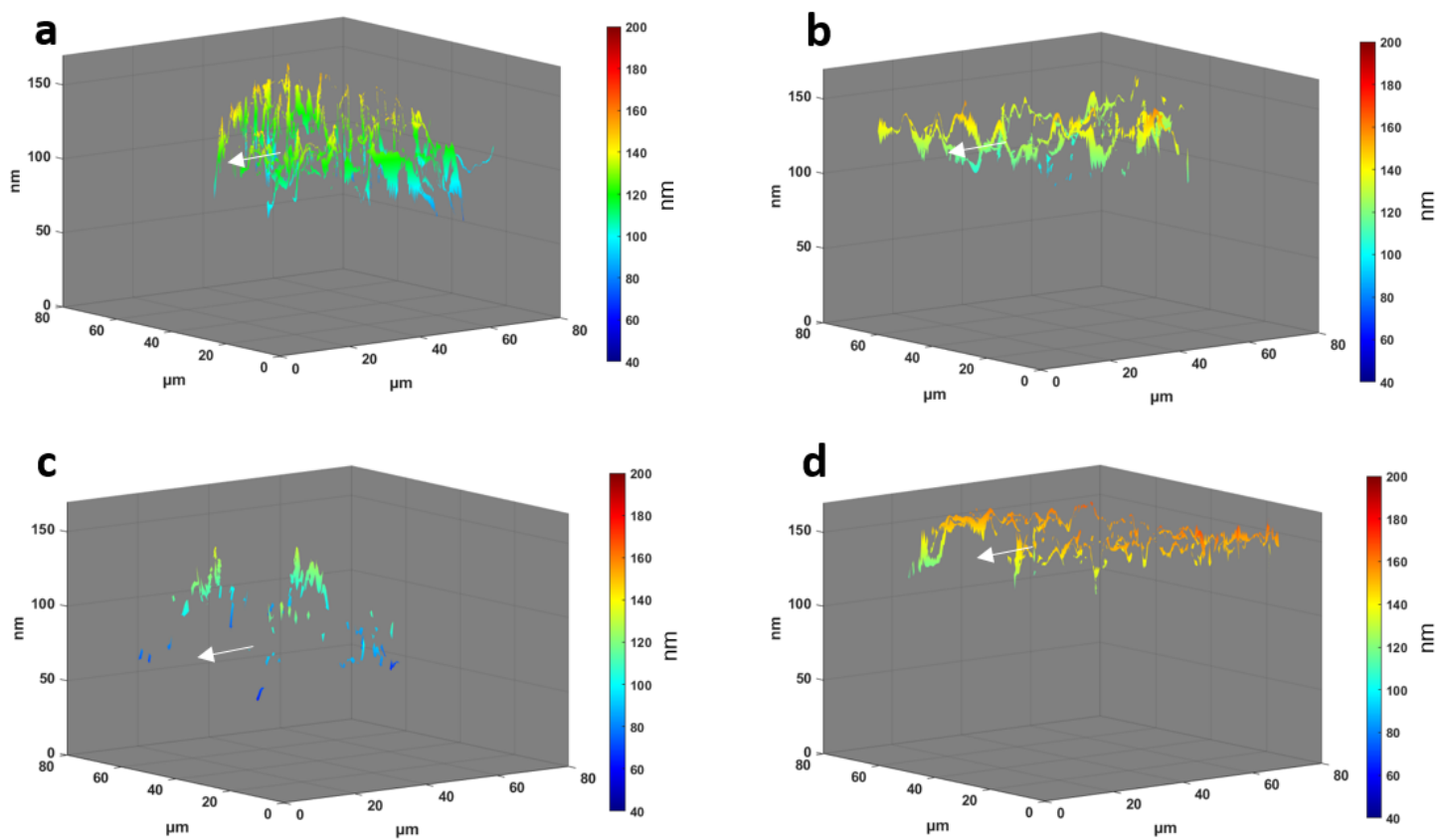
**Figure 2**

Converting Fluorescence Lifetime to Height Values for further Analysis. a. Untreated cell: FLIM image, intensity weighted height image of the actin cytoskeleton, extracted stress fiber height image, actin edge image. b. Blebbistatin treated cell: FLIM image, intensity weighted height image of the actin cytoskeleton, extracted stress fiber height image, actin edge image. c. Y27632 treated cell: FLIM image, intensity weighted height image of the actin cytoskeleton, extracted stress fiber height image, actin edge image. d. Rho Activator treated cell: FLIM image, intensity weighted height image of the actin cytoskeleton, extracted stress fiber height image, actin edge image. The white arrow shows the polarity of the cell.



**Figure 3**

Height analysis of the actin cytoskeleton. Each dot represents the median of a single cell. a. Height of Actin of untreated and Blebbistatin, Y27632, Rho Activator treated cells. b. Height of stress fibers of untreated cells and cells treated with Blebbistatin, Y27632 and Rho Activator. c. 10th percentile of stress fiber height of actin of untreated and Blebbistatin, Y27632, Rho Activator treated cells. d. 90th percentile of stress fiber height of untreated cells and cells treated with Blebbistatin, Y27632 and Rho Activator. e. Median of 10th percentile versus median of 90th percentile stress fiber height of untreated and Blebbistatin, Y27632, Rho Activator treated cells. f. Relative stress fiber rise is the normalized difference of the 90th to 10th percentile of stress fiber height. Test: Wilcoxon-rank sum. ns:  $p > 0.05$ , \*:  $p \leq 0.05$ , \*\*:  $p \leq 0.01$ , \*\*\*:  $p \leq 0.001$ , \*\*\*\*:  $p \leq 0.0001$ .

**Figure 4**

3 D plots of the actin distribution with height information in z dimension. The arrow represents the polarization of the cell. The cells shown are the cells from figure 2 and representative of their population. a. Untreated cells. b. Blebbistatin treated cells. c. Y27632 treated cells. d. Rho Activator treated cells.

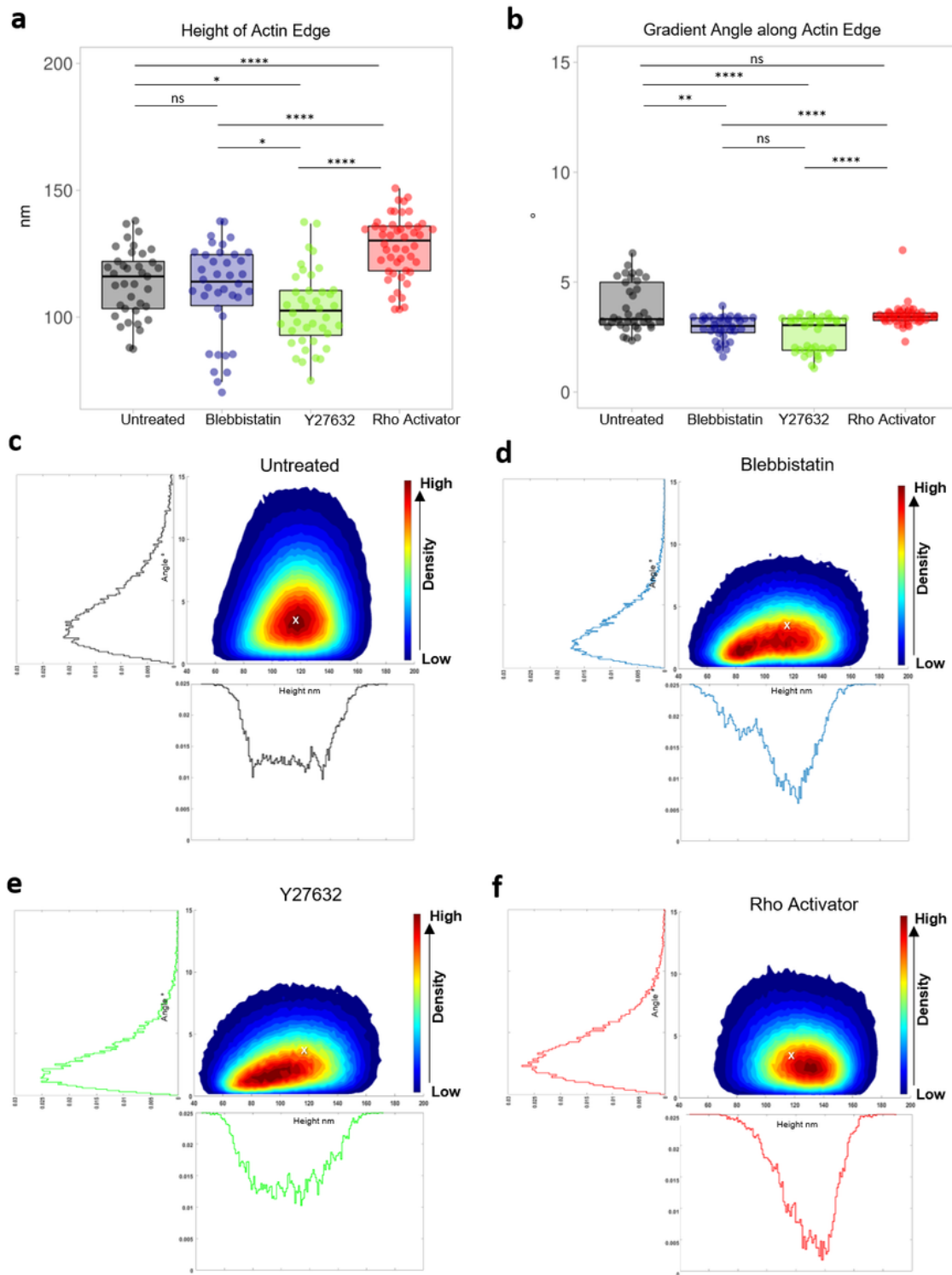


**Figure 5**

Actin edge analysis. a. Height of actin edge of untreated and Blebbistatin, Y27632, Rho Activator treated cells. Each dot represents the median of a single cell. b. Gradient angle along actin edge of untreated cells and cells treated with Blebbistatin, Y27632 and Rho Activator. Each dot represents the median of a single cell. Test: Wilcoxon-rank sum. ns:  $p > 0.05$ , \*:  $p \leq 0.05$ , \*\*:  $p \leq 0.01$ , \*\*\*:  $p \leq 0.001$ , \*\*\*\*:  $p \leq 0.0001$ . Contour of the scatter plot of the height of actin edge and the gradient angle along actin edge.

The colormap indicates the density. Histogram of the gradient angle along the actin edge and histogram of the height of actin edge. c. Untreated cells. d. Rho Activator treated cells. e. Blebbistatin treated cells. f. Y27632 treated cells. The white cross in Plot C-F shows the maximum of the untreated cell.

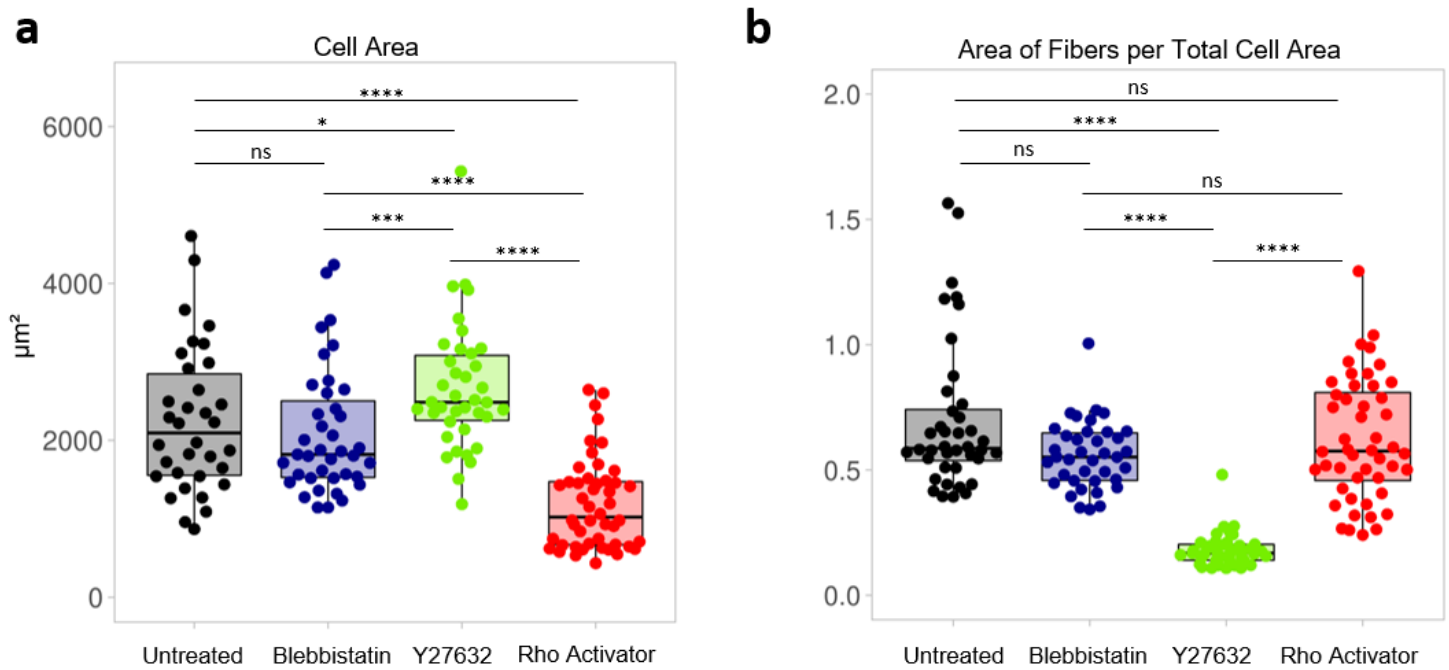


**Figure 6**

Focal plane analysis. Each dot represents the median of a single cell. a. Cell area of untreated and Blebbistatin, Y27632, Rho Activator treated cells. b. Area of actin fibers per total cell area of untreated cells and cells treated with Blebbistatin, Y27632 and Rho Activator. Test: Wilcoxon-rank sum. ns:  $p > 0.05$ , \*:  $p \leq 0.05$ , \*\*:  $p \leq 0.01$ , \*\*\*:  $p \leq 0.001$ , \*\*\*\*:  $p \leq 0.0001$ .

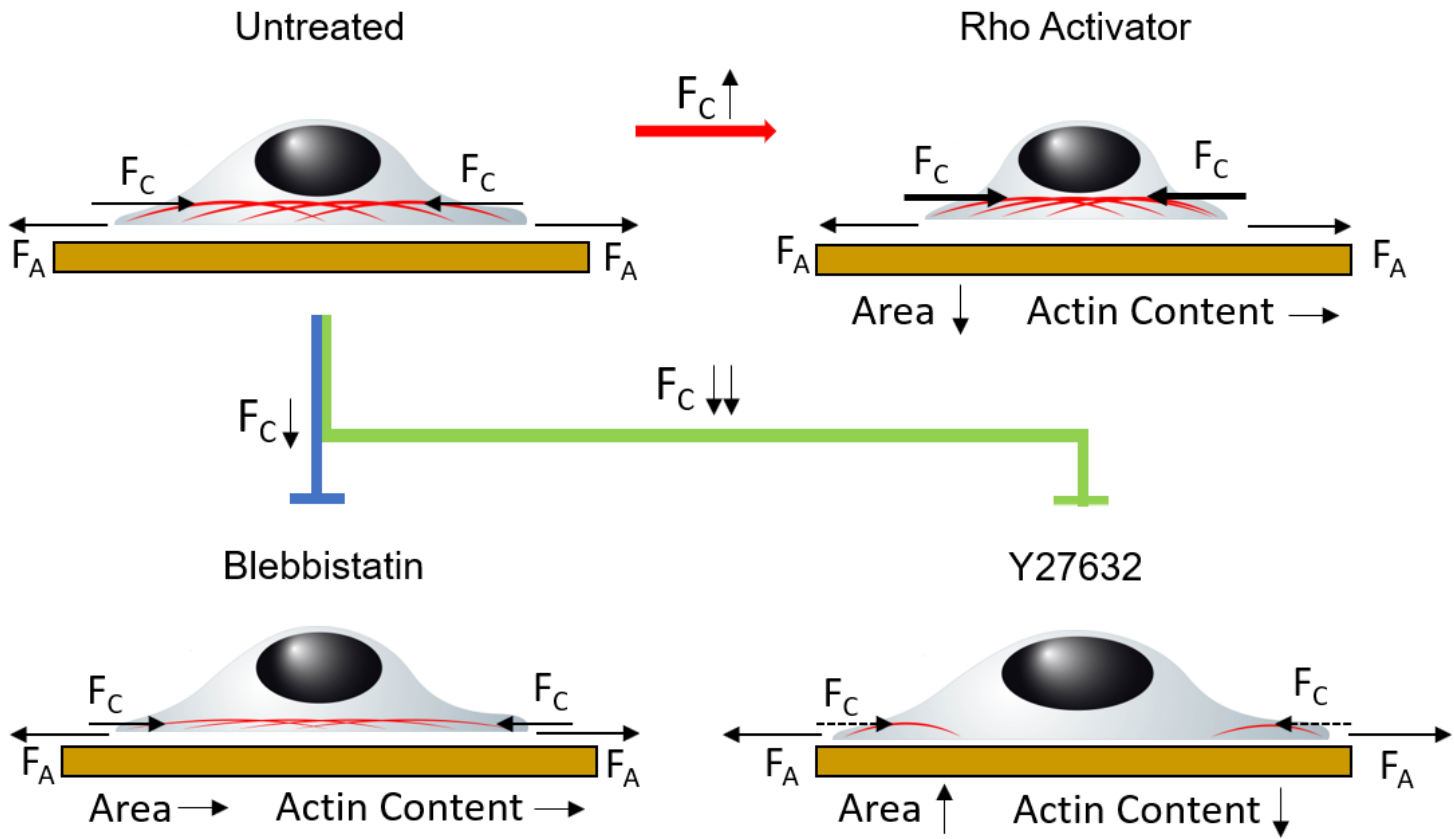


**Figure 7**

Application of the model of equilibrium between adhesion tension  $F_A$  and cytoskeleton tension  $F_C$  in untreated cells. Treatment with Blebbistatin and Y27632 as inhibitors and Rho Activator as promoter changes the cytoskeleton tension and leads to an imbalance. This changes the height of the actin cytoskeleton and the morphology.

**Image not available with this version**

**Figure 8**

Figure 8 not available with this version